

# Analysis of LIDAR Data Fused with Co-Registered Bands

Marc Bartels, Hong Wei and James Ferryman

Computational Vision Group, School of Systems Engineering

The University of Reading

Whiteknights, Reading, RG6 6AY, United Kingdom

m.bartels@reading.ac.uk, h.wei@reading.ac.uk

<http://www.cvg.reading.ac.uk/projects/LIDAR>

## Abstract

*In the past decade, Light Detection And Ranging (LIDAR) has been recognised by both the commercial and public sector as a reliable and accurate source for land surveying. Object classification in LIDAR data tends towards data fusion by employing additional simultaneously recorded bands. In this paper, a rule-based approach is presented for improving classification accuracy obtained in a supervised Maximum Likelihood classification. Simultaneously recorded co-registered bands are used such as high resolution LIDAR first, last echo and intensity data, aerial and near infra-red photos. Issues regarding feature and class selection and differentiated accuracy assessment are addressed. Furthermore, the individual influence of each band on the classification is investigated. The results show that incorporating additional knowledge and considering contextual relationships among classes is beneficial for improving classification accuracy in fused LIDAR datasets.*

## 1. Introduction

Light Detection And Ranging (LIDAR) for terrain and land surveying has made significant contributions to many environmental, engineering and civil applications. It is therefore not surprising that LIDAR data is being used increasingly by the public and commercial sector since the early 1990s [1]. Applications such as forestry, building reconstruction, flood modelling and corridor mapping are based on post processing of LIDAR data point clouds, as they are accurate for less hilly terrain [2]. Mounted on an airborne platform, a LIDAR data acquisition system estimates the distance between the instrument and a point on the surface by measuring the time the laser pulse needs to return [2]. A Global Positioning System (GPS) receiver and an Inertial Navigation System (INS) complement the data with position and orientation, respectively [2].

In one of the early investigations on height of LIDAR data, Weidner and Förstner [3] separated ground and object points in estimating a normalised Digital Surface Model (nDSM) by subtracting a morphologically filtered Digital Terrain Model (DTM) from the original Digital Surface Model (DSM). An approach to model buildings from LIDAR data in a less sloped area was developed by Maas *et al.* [4], sub-divided into two parts. First, a texture based segmentation employing Maximum Likelihood (ML) applied to LIDAR data and two further height derived bands [5, 6] and second, the actual modelling of the buildings from the point cloud [7]. Bretar *et al.* [8] segmented roofs in ungridded original LIDAR data point clouds merging aerial images where the authors challenged the difficulty of irregular distributed LIDAR points successfully. Bartels *et al.* [9] developed *Skewness Balancing*, a statistical method to separate object and ground points based on the LIDAR point cloud's distribution.

In the course of increasing the LIDAR data resolution and the possibility of recording complementary bands, researchers developed further classification techniques using data fusion. Realistic 3D city models from LIDAR data were presented by Brenner and Haala *et al.* [10, 11] who reconstructed buildings, facades and vegetation using multiple data sources, such as near infra-red and terrestrially captured images [12]. The building ground planes were estimated with a 2D GIS map complemented with a cadastral map. Building reconstruction by fusing LIDAR data and aerial photos was presented by Rottensteiner *et al.* [13]. First, the authors detected building regions in ungridded data. Then, roofs were detected using a curvature-based segmentation technique and additional planar surfaces were estimated from aerial photos. Supervised parametric classification based on the Gaussian mixture model and Expectation Maximisation was used by Charaniya *et al.* [14] to classify roads, roofs, trees and grass in LIDAR data using data fusion with an nDSM, intensity data, height variation, difference of first and last echo and a grey scale aerial photo.

This paper presents a rule-based refinement for accuracy improvement of supervised classification using ML of high resolution LIDAR first echo, last echo and LIDAR intensity data and co-registered line scanner bands such as aerial and near infra-red photo. Buildings, vegetation, cars and ground are classified. It is commonly agreed that the accuracy of ML is limited. For this reason, contextual knowledge is used to improve the results by exploiting the inter-class relationships. Furthermore, individual impact of feature combination on the classification result is analysed. The theoretical background is derived in Section 2. Section 3 presents the multivariate features and introduces the classes. Section 4 discusses the accuracy assessment approach, while results are discussed in Section 5. The paper concludes and outlines future work in Section 6.

## 2. Theoretical Background

### 2.1. Maximum Likelihood (ML)

The ML classifier is suitable for multivariate problems involving multiple simultaneously recorded bands [15]. Fusing LIDAR data and co-registered channels yields a  $D$  dimensional feature space  $\mathbf{F}$  of size  $M \times N$ . Given class  $\Omega_i$ ,  $i \in \{1, 2, \dots, R\}$ , where  $R$  is the number of classes, the probability of a pixel represented by its feature vector  $\vec{f}_{x,y} \in \mathbf{F}$  at position  $(x, y) \in \{M \times N\}$  actually belonging to class  $\Omega_i$ , is defined by the Bayes' rule [16]:

$$P(\Omega_i | \vec{f}_{x,y}) = \frac{P(\vec{f}_{x,y} | \Omega_i) P(\Omega_i)}{P(\vec{f}_{x,y})} \quad (1)$$

where  $P(\Omega_i)$  and  $P(\vec{f}_{x,y})$  are the prior probabilities of class  $\Omega_i$  and the pixel represented by the feature vector  $\vec{f}_{x,y}$ , respectively. By estimating  $P(\Omega_i | \vec{f}_{x,y})$ , the lack of knowledge of these two prior probabilities can be bypassed by assuming both to be uniformly distributed for all channels [15]. Therefore, Equation (1) can be reduced to

$$P(\Omega_i | \vec{f}_{x,y}) \propto P(\vec{f}_{x,y} | \Omega_i) \quad (2)$$

Another important assumption is that measured natural samples, such as  $\mathbf{F}$ , are Gaussian distributed as stated by the *central limit theorem* [17]. Thus,  $P(\vec{f}_{x,y} | \Omega_i)$  on the right hand side of Equation (2) can be defined as [17]

$$P(\vec{f}_{x,y} | \Omega_i) = \frac{1}{\sqrt{2\pi}^D \sqrt{|\mathbf{C}_i|}} e^{-\frac{1}{2}M} \quad (3)$$

with  $M$  as the squared Mahalanobis distance [17]

$$M = (\vec{f}_{x,y} - \vec{\mu}_i)^T \mathbf{C}_i^{-1} (\vec{f}_{x,y} - \vec{\mu}_i) \quad (4)$$

where  $\vec{\mu}_i$  denotes the mean vector and  $\mathbf{C}_i$  the  $D \times D$  covariance matrix of class  $\Omega_i$ , with  $|\mathbf{C}_i|$  and  $\mathbf{C}_i^{-1}$  as its determinant and inverse, respectively [18]. For notation purposes,  $T$  refers to transposing vector  $(\vec{f}_{x,y} - \vec{\mu}_i)$ . Equation (3) can be further simplified as

$$\ln(P(\vec{f}_{x,y} | \Omega_i)) = -\frac{D}{2} \ln(2\pi) - \frac{1}{2} \ln|\mathbf{C}_i| - \frac{1}{2}M \quad (5)$$

Since the term  $-\frac{D}{2} \ln(2\pi)$  is constant for all classes it can be discarded from Equation (5). Multiplying the remaining terms in Equation (5) with the factor  $-2$  results in

$$\tilde{P}(\vec{f}_{x,y} | \Omega_i) = -2 \ln(P(\vec{f}_{x,y} | \mathbf{C}_i)) = \ln|\mathbf{C}_i| + M \quad (6)$$

$\tilde{P}$  as denoted in Equation (6) is calculated for each pixel and each class. Finally, after normalisation,  $\tilde{P}$  has to be *minimised* to obtain a labelled classified image.

### 2.2. Rule-based Classification Refinement

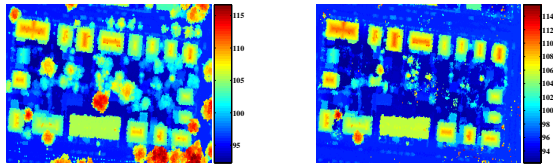
In order to reduce false positives in an ML classification, the spatial context of the classes and their relation among each other is incorporated. Considering the spatial resolution of LIDAR data -  $0.5m$  per pixel - as used in this study, the following rules are derived.

- The edges of the smallest objects, cars, are expected to cover at least an area  $0.5m^2$ , equivalent to  $2 \times 1$  pixels in either direction. Therefore, none of the detected objects can be smaller than two pixels. For this reason, single pixels are flipped into the majority of their adjacent pixels in a  $3 \times 3$  neighbourhood.
- No object can be within a hard opaque object such as cars and buildings. For example, cars cannot be within buildings and vice versa. Likewise, vegetation cannot be within a car or a building. Misclassified pixels within those hard objects of an area  $1m^2$  or  $2 \times 2$  pixels within a  $4 \times 4$  window can therefore be assumed to have actually the circumjacent pixel value.
- Conventional cars cannot exceed an area of  $5.5m^2$  or 22 pixels. Thus, if the number of clustered pixels representing cars in a  $5 \times 5$  environment is greater than 22, they are flipped to buildings as the probability is high that they are actually building pixels.
- Buildings do not occupy an area less than  $5.5m^2$ . Therefore, if the area of a building is less than  $1m^2$  and the area of a car is greater than  $1m^2$  in a  $5 \times 5$  environment, building pixels are corrected to car pixels.

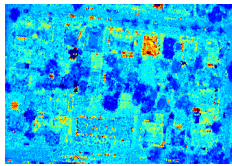
### 3. Feature Space and Classes

#### 3.1. Feature Space

Three LIDAR bands and two co-registered line scanner photos are employed in this study as shown in Figure 1. All channels are recorded simultaneously and cover an area of  $0.019km^2$ . The LIDAR first echo DSM (FE) in Figure 1(a) is a height profile of the scene and resolves *detached objects* (both hard and soft) such as buildings, sheds, trees and bushes. The LIDAR last echo (LE) in Figure 1(b) is a representation of the scene after the laser has penetrated soft objects such as deciduous vegetation. Both LIDAR echoes are reported to have a high vertical accuracy, especially in less hilly terrain [2]. Additionally, LIDAR data neither contains shadows nor surface texture. LIDAR intensity data (INT) in Figure 1(c) represents the amount of power returning to the LIDAR recording device and can distinguish among objects of similar height but different absorbing characteristics, such as water and tarmac. Bands of the aerial (RGB) and near infra-red (NIR) photos in Figure 1(d) and 1(e), respectively, contribute spectral characteristics which are beneficial for describing vegetation and other heat emitting objects. Table 1 lists all wavelengths of the employed bands.



(a) First echo DSM in metres (FE) (b) Last echo DSM in metres (LE)



(c) 8-bit LIDAR intensity data (INT)



(d) 8-bit aerial photo (RGB)



(e) 8-bit near infra-red photo (NIR)

**Figure 1. LIDAR data and co-registered bands**

Band	Wavelength in <i>nm</i>
LIDAR first echo (FE)	1560
LIDAR last echo (LE)	1560
Red channel of aerial photo (R)	580 – 660
Green channel of aerial photo (G)	500 – 580
Blue channel of aerial photo (B)	450 – 490
Near infra-red photo (NIR)	770 – 890

**Table 1. Features' spectral characteristics**

When selecting features, the determinant  $|C_i|$  of the covariance matrix of  $\Omega_i$  has to be non-singular, *i.e.*  $|C_i| \neq 0$  has to be satisfied in order to calculate  $C_i^{-1}$ . Consequently, the feature vectors have to be linearly independent of each other [18]. Otherwise, redundant features have to be removed from or compensated in  $F$  [15]. In this study, two channel pairs are correlated: first, the red channel of the aerial photo and the green channel of the NIR photo; second, the green channel of the aerial photo and the blue channel of the NIR photo. Thus, both the green and the blue channel of the NIR photo are removed from  $F$  to achieve  $|C_i| \neq 0$ .

#### 3.2 Classes

Four distinctive classes are defined: building, vegetation, car and ground. At this stage, trees, low vegetation and grass are summarised as vegetation. High buildings and sheds are generalised as class building. In the LIDAR community, the first two classes (building, vegetation) are referred as *detached objects* [19] and the fourth class (ground), including the top layer soil, thin man-made layering such as asphalt or tarmac are defined as *bare earth* [19]. Defining the class car is justified because cars can be spotted in the high resolution data set at  $0.5m$  per pixel. They are clearly visible in bands penetrating canopies of deciduous vegetation, *i.e.* the LIDAR last echo in Figure 1(b) and the line scanner data in Figures 1(d) and 1(e). Though not permanently situated in a scene, those cars still have to be removed when generating DTMs or nDSMs as discussed in Section 1.

### 4 Accuracy Assessment

Based on the ground truth, a confusion matrix can be produced to assess the classification accuracy. The overall accuracy can be estimated by the ratio of the sum of its main diagonal and the total number of classified pixels [15]. Examining individual classes, producer's and user's accuracy can be calculated. The producer's accuracy evaluates the proportion of correctly classified pixels from the collected class samples, and is estimated for each class by the ratio of its diagonal element and the sum of its columns [15]. The

user's accuracy stands for the proportion of pixels which were correctly assigned to one particular class, estimated for each class by the ratio of the diagonal element and the sum of its row [15].

The overall accuracy takes only the correctly classified pixels into account. Alternatively, another multivariate measure  $\kappa$  (kappa) examines the whole confusion matrix including its off-diagonal elements. In this way,  $\kappa$  is a representation of classification accuracy closer to a more global statement and is defined as [15]

$$\kappa = \frac{\theta_1 - \theta_2}{1 - \theta_2} \quad (7)$$

$$\theta_1 = \frac{1}{(M \times N)} \sum_{r=1}^R x_{rr} \quad (8)$$

$$\theta_2 = \frac{1}{(M \times N)^2} \sum_{r=1}^R x_{r+} \cdot x_{+r} \quad (9)$$

where  $x_{rr}$  represents the diagonal elements of the confusion matrix at index  $r$  and  $x_{r+}$  and  $x_{+r}$  are the sum of row  $r$  and column  $r$ , respectively.

## 5. Results and Discussion

### 5.1. Feature Space Analysis

The influence of each band on the classification result is investigated by construction feature spaces using each of the seven combinations of the three LIDAR bands first echo (FE), last echo (LE) and intensity data (INT) as indicated by blue bars in Figure 2. The second analysis with the same LIDAR band combinations takes additionally the aerial (RGB) and near infra-red photo (NIR) into account as depicted with red bars in Figure 2.

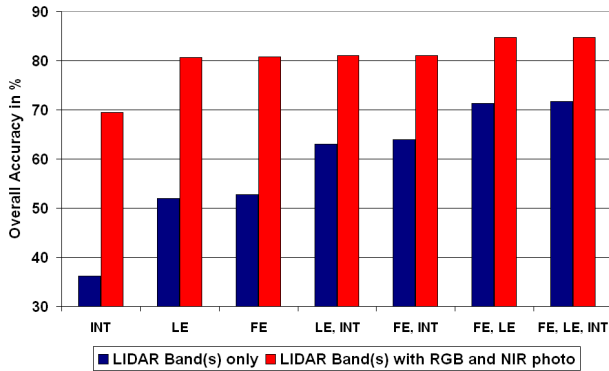


Figure 2. Feature space analysis

Referring to the fundamental analysis (blue bars), *i.e.* the impact of the LIDAR bands on the results only, the following findings can be stated:

- The poorest accuracy of 36.13% is obtained using LIDAR intensity data (INT) alone which acts as a baseline for further reference.
- LIDAR first (FE) *or* last echo (LE), respectively, have a much stronger influence by a difference of  $\Delta 15.83\%$  compared to LIDAR intensity data (INT).
- However, LIDAR intensity data (INT) is still useful as it increases the classification result of LIDAR first echo (FE) *or* last echo (LE) by  $\Delta 26.94\%$ .
- The highest score for the basic experiment is achieved by a combination of LIDAR first echo (FE) *and* last echo (LE). Using both echoes as a feature space, an improvement of  $\Delta 35.25\%$  compared to LIDAR intensity data (INT) is achieved.
- Finally, including LIDAR intensity data (INT) does not increase the accuracy significantly by only  $\Delta 0.30\%$  compared to the combination of the LIDAR echoes.

The same feature space investigation is carried out using the additional recorded bands on top of the seven combinations (red bars), *i.e.* the aerial (RGB) and the near infra-red (NIR) photo. Apart from confirming the basic findings, further conclusions can be drawn:

- Incorporating additionally the co-registered bands, the overall accuracy improvement ranges between  $\Delta 13.31\%$  and  $\Delta 33.33\%$ .
- The poor performance of LIDAR intensity data (INT) is compensated by these additional bands: while the accuracy of LIDAR first echo (FE) *or* last echo (LE) increases with the LIDAR intensity data (INT) in the fundamental analysis (blue bars), this band is no longer required when incorporating both photos (red bars) as it does not affect the results.

### 5.2. Incorporating Contextual Knowledge

All five bands as introduced in Section 3.1 are used for feature space construction because they produce the highest scores as analysed in Section 5.1. Figure 4 depicts the ML classification result, the successive rule-based improvement and the ground truth. It can be seen that *detached objects*, *i.e.* buildings (black) and vegetation (green) and cars (red) are categorised. Even grass is correctly classified despite its insignificance towards the height information in LIDAR data. Hence, as expected, line scanner bands have more impact on detecting grass and low vegetation. Class ground as

*bare earth* (white) also shows a good response to the classifier despite its various appearance as top layer soil, thin man-made layering such as asphalt or tarmac. The overall accuracy for the results in Figure 4(a) from the confusion matrix in Table 2 (top) is about 84.80% and  $\kappa \approx 77.34\%$ .

		Ground Truth				
		B	V	C	G	Total
Classified Data	B	<b>17493</b>	797	198	1726	20214
	V	1801	<b>24032</b>	118	1990	27941
	C	246	42	<b>334</b>	331	953
	G	1546	2247	372	<b>21843</b>	26008
	Total	21086	27118	1022	25890	<b>75116</b>

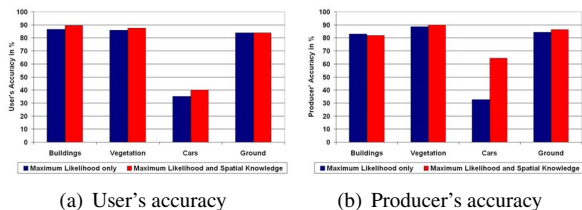
  

		Ground Truth				
		B	V	C	G	Total
Classified Data	B	<b>18070</b>	563	83	1498	20214
	V	1903	<b>24420</b>	16	1602	27941
	C	220	1	<b>382</b>	350	953
	G	1868	2185	111	<b>21844</b>	26008
	Total	22061	27169	592	25294	<b>75116</b>

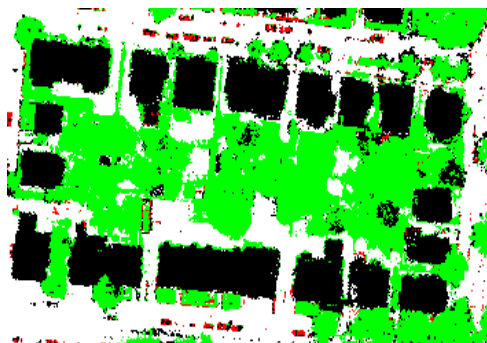
**Table 2. Confusion matrices before (top) and after (bottom) rule-based corrections; B = Building, V = Vegetation, C = Car, G = Ground**

However, it can also be seen that there is a number of false positives for each class due to their ambiguity among the features in  $F$  as discussed in Section 3.1. Another reason is that there is only a limited number of cars present in the scene. Consequently, errors have a stronger impact on the accuracy of class car than on other classes. These misclassified pixels are corrected by employing contextual information as introduced in Section 2.2. The improved result is shown in Figure 4(b) and from confusion matrix in Table 2 (bottom), an overall accuracy of approximately 86.15% and a  $\kappa$  of about 79.33% is achieved.

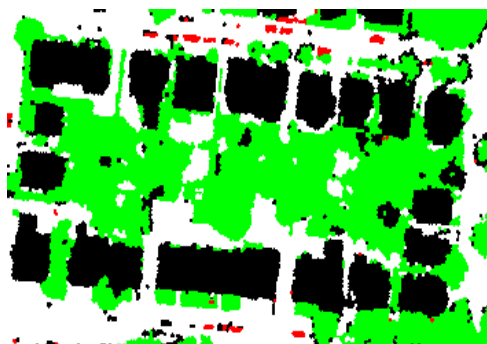
Figure 3 depicts the user’s and producer’s accuracies after ML classification before and after rule-based refinement. Both accuracies of classes building, vegetation and ground range between 81.91% and 89.88% and remain fairly stable. However, the user’s and producer’s accuracies of class car are improved by about 5.03% and 31.85%, respectively, by incorporating spatial knowledge.



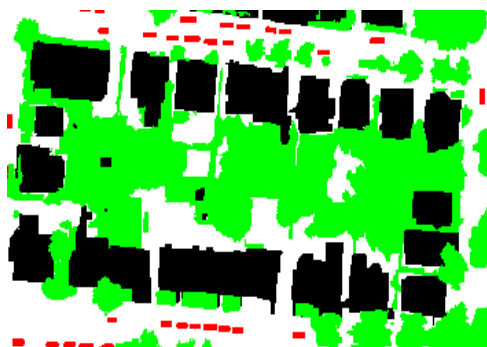
**Figure 3. User’s and producer’s accuracies before and after accuracy improvement**



(a) ML classification



(b) Improved results incorporating contextual knowledge



(c) Ground truth

**Figure 4. Results and ground truth: building (black), vegetation (green), car (red) and ground (white)**

## 6. Conclusions and Future Work

In this paper, a rule-based approach is presented to improve of parametric supervised classification with ML applied to LIDAR data using data fusion. To construct an appropriate feature space, LIDAR first and last echo, intensity data and simultaneously recorded co-registered bands such as aerial and near infra-red photos are employed.

Four classes are classified and their individual accuracy is assessed. The results show that *detached objects* (buildings, vegetation), cars and *bare earth* are correctly classified. False positives are significantly reduced by using a rule-based approach which incorporates contextual knowledge and inter-class relationships. Outstanding is the producer's accuracy improvement of class car which is superior to a simple ML classification by about 32%.

The individual influence of each band on the classification is assessed with the following findings: LIDAR intensity data has the lowest impact, LIDAR first *or* last echo data alone produce higher scores and have similar influence either alone or with LIDAR intensity data. However, LIDAR first *and* last echo combined yield the strongest results which cannot be significantly improved even with LIDAR intensity data. Further investigations showed that additional aerial and near infra-red bands reinforce the accuracy and compensate the poor performance of LIDAR intensity data.

For future work, the classification approach will be improved by introducing additional uncorrelated features, *e.g.* Normalised Difference Vegetation Index (NDVI) and further height derived features such as the difference between LIDAR first and last echo; mean, standard deviation, variation, gradient of LIDAR first echo. The use of Gabor filters [20, 21] and wavelets [22, 23] will also be examined for feature extraction. Further investigation will also focus on expanding the developed algorithm to different scenes in order to categorise more classes.

## Acknowledgements

The project is RETF funded by the University of Reading. The authors would like to thank TopoSys GmbH, and the Stadt Mannheim, Germany, for LIDAR data supply.

## References

- [1] H.-G. Maas. Akquisition von 3D-GIS Daten durch Flugzeuglaser-scanning. *Kartographische Nachrichten*, 55(1):3–11, 2005.
- [2] E. J. Huising and L. M. Gomes Pereira. Errors and accuracy estimates of laser data acquired by various laser scanning systems for topographic applications. *ISPRS Journal of Photogrammetry & Remote Sensing*, 53:245–261, 1998.
- [3] U. Weidner and W. Förstner. Towards Automatic Building Extraction from High Resolution Digital Elevation Models. *ISPRS Journal of Photogrammetry & Remote Sensing*, 50(4):38 – 49, 1995.
- [4] H.-G. Maas and G. Vosselman. Two algorithms for extracting building models from raw laser altimetry data. *ISPRS Journal of Photogrammetry & Remote Sensing*, 54:153–163, 1999.
- [5] H.-G. Maas. Fast determination of parametric house models from dense airborne laserscanner data. *International Workshop on Mobile Mapping Technology*, 32(2W1):1–6, 1999.
- [6] H.-G. Maas. The potential of height texture measures for the segmentation of airborne laserscanner data. *Fourth International Airborne Remote Sensing Conference and Exhibition / 21st Canadian Symposium on Remote Sensing*, I:154–161, 1999.
- [7] H.-G. Maas. Closed solutions for the determination of parametric building models from invariant moments of airborne laserscanner data. *ISPRS Conference on Automatic Extraction of GIS Objects from Digital Imagery*, 32(3-2W5):193–199, 1999.
- [8] Frédéric Bretar, Marc Pierrot-Deseilligny, and Michel Roux. Recognition of Building Roof Facets by Merging Aerial Images and 3D Lidar Data in a Hierarchical Segmentation Framework. *18th International Conference on Pattern Recognition*, IV:5–8, 2006.
- [9] M. Bartels, H. Wei, and D. C. Mason. DTM Generation from LIDAR Data using *Skewness Balancing*. *18th International Conference on Pattern Recognition*, I:566–569, 2006.
- [10] N. Haala and C. Brenner. Generation of 3D city models from airborne laser scanning data. *EARSEL Workshop on LIDAR remote sensing of land and sea*, pages 105–112, 1997.
- [11] N. Haala and C. Brenner. Fast Production of Virtual Reality City Models. *International Archives of Photogrammetry and Remote Sensing*, 32(4):77–84, 1998.
- [12] N. Haala, C. Brenner, and C. Staetter. An integrated system for urban model generation. *Proceedings ISPRS Congress Commission II, Working Group 6*, pages 96–103, 1998.
- [13] F. Rottensteiner and C. Briese. Automatic generation of building models from LIDAR data and the integration of aerial images. *International Archives of the Photogrammetry, Remote Sensing and Spatial Information Sciences of the ISPRS*, 34(3/W13):174 – 180, 2003.
- [14] A. P. Charaniya, R. Manduchi, and S. K. Lodha. Supervised Parametric Classification of Aerial LiDAR Data. *IEEE Conference on Computer Vision and Pattern Recognition Workshop*, pages 30 – 38, 2004.
- [15] B. Tso and P. M. Mather. *Classification Methods for Remotely Sensed Data*. London: Taylor & Francis, 2001.
- [16] F. V. Jensen. *Bayesian Networks and Decision Graphs*. New York: Springer-Verlag, 2001.
- [17] R. O. Duda, P. E. Hart, and D. G. Stork. *Pattern classification*. New York: Wiley, 2001.
- [18] I. L. Thomas, V. M. Benning, and N. P. Ching. *Classification of Remotely Sensed Images*. Bristol: Adam Hilger, 1987.
- [19] G. Sithole and G. Vosselman. Automatic structure detection in a point cloud of an urban landscape. *Proceedings of 2nd Joint Workshop on Remote Sensing and Data Fusion over Urban Areas (Urban 2003)*, pages 67–71, 2003.
- [20] H. Wei and M. Bartels. Gabor Wavelets and Gaussian Models to Separate Ground and Non-ground for Airborne Scanned LIDAR Data. *4th International Workshop on Pattern Recognition in Remote Sensing, in conjunction with International Conference on Pattern Recognition*, I:9–12, 2006.
- [21] H. Wei and M. Bartels. Unsupervised Segmentation Using Gabor Wavelets and Statistical Features in LIDAR Data Analysis. *18th International Conference on Pattern Recognition*, I:667–670, 2006.
- [22] M. Bartels and H. Wei. Towards DTM Generation from LIDAR Data in Hilly Terrain using Wavelets. *4th International Workshop on Pattern Recognition in Remote Sensing, in conjunction with International Conference on Pattern Recognition*, I:33–36, 2006.
- [23] M. Bartels, H. Wei, and D. C. Mason. Wavelet Packets and Co-occurrence Matrices for Texture-based Image Segmentation. *IEEE International Conference on Advanced Video and Signal-Based Surveillance*, 1:428–433, 2005.